Ultrabroadband and Wide-Angle Hybrid Antireflection Coatings With Nanostructures

Emmett E. Perl, Chieh-Ting Lin, William E. McMahon, Daniel J. Friedman, and John E. Bowers

***Abstract*—Ultrabroadband and wide-angle antireflection coatings (ARCs) are essential to realizing efficiency gains for state-of-the-art multijunction photovoltaic devices. In this study, we examine a novel design that integrates a nanostructured antireflection layer with a multilayer ARC. Using optical models, we find that this hybrid approach can reduce reflected AM1.5D power by 10–50 W/m^2 over a wide angular range compared to conventional thin-film ARCs. A detailed balance model correlates this to an improvement in absolute cell efficiency of 1–2%. Three different ARC designs are fabricated on indium gallium phosphide, and reflectance is measured to show the benefit of this hybrid approach.**

***Index Terms*—Biomimetics, optical films, photovoltaic cells, III–V semiconductor materials.**

I. Introduction

FOR nearly two decades, multijunction solar cells have had the highest efficiencies of all photovoltaic technologies. Current three-junction (3-J) architectures have achieved efficiencies as high as 44.4% under concentration, and the development of four-junction (4-J) and five-junction (5-J) devices will put the industry within striking distance of attaining 50% conversion efficiency [1], [2].

State-of-the-art multijunction cells are based on III–V materials, which reflect around 30% of incident light due to the high index of refraction of these compounds. A standard two-layer antireflection coating (ARC) is usually sufficient to reduce the impact of reflection for most 3-J devices, even when reflectivity increases at long wavelengths.

This is especially true for germanium-based 3-J devices because high infrared (IR) reflectivity will not affect a 0.66-eV lower junction as long as it remains oversupplied with photons. For 3-J devices that use a bottom junction with a bandgap closer to 1.0 eV, IR requirements are not as intense since the cell will absorb a narrower range of wavelengths [3].

However, 4-J and 5-J devices incorporating additional low bandgap materials have become competitive with state-of-the-art 3-J cells. These designs are more constrained and require ARCs with consistently low-power reflection over a wavelength range from about 300–1800 nm [1], [4]–[6].

One common approach to reduce reflections over a two-layer coating is to deposit more ARC layers onto the sample. However, these multilayer designs are ultimately constrained by the availability of suitable low-index ($n < 1.4$) and low-loss high-index ($n > 2.5$) materials.

An alternative approach makes use of antireflective nanostructures, which consist of subwavelength protrusions originally discovered on the surface of a moth-eye to minimize visibility to predators. If these nanostructures are tapered, incoming light will see a smooth gradient in the effective index of refraction. With no abrupt interfaces, Fresnel reflections are greatly reduced and near-zero reflectance over a broad range of wavelengths and angles is possible [7], [8].

Antireflective nanostructures have been integrated with III–V photovoltaic devices using various approaches [9]–[15]. However, it is difficult to incorporate these structures without introducing additional loss mechanisms. Direct patterning of the active device is usually coupled with cell damage [9], [10]. This can be avoided by placing the nanostructures into a thickened AlInP window layer. However, this will lead to a significant increase in absorption at short wavelengths [11]–[13]. Etching nanostructures into a low-loss dielectric layer can minimize this absorption, but will introduce a large gap in the refractive index between the dielectric and semiconductor, leading to an increase in reflection [14], [15].

Here, we report on a novel design that integrates a nanostructured antireflection layer with an interference-based ARC. Fig. 1 illustrates this hybrid approach, showing the cross-sectional structure and correlated effective index of refraction of the design. The moth-eye coupling layer efficiently transmits light from air into a low-loss dielectric layer, and the multilayer

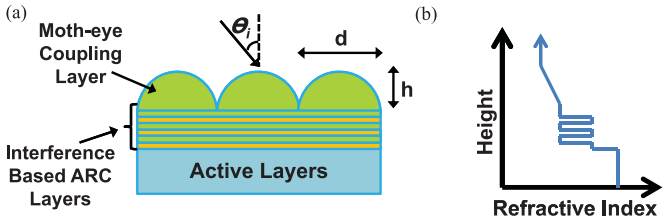

Fig. 1. (a) Diagram of the hybrid ARC design. (b) Effective index of refraction versus height for the full antireflective structure.

Manuscript received July 26, 2013; revised December 5, 2013; accepted January 22, 2014. Date of publication February 21, 2014; date of current version April 18, 2014. This work was supported primarily by the Center for Energy Efficient Materials, which is an Energy Frontier Research Center funded by the U.S. Department of Energy, Office of Science, Office of Basic Energy Sciences, under Award DE-SC0001009. The work of E. E. Perl was supported by the National Science Foundation Graduate Research Fellowship under Grant DGE-1144085.

E. E. Perl, C.-T. Lin, and J. E. Bowers are with the Department of Electrical and Computer Engineering, University of California at Santa Barbara, Santa Barbara, CA 93106 USA (e-mail: emmettperl@ece.ucsb.edu; clin01@umail.ucsb.edu; bowers@ece.ucsb.edu).

W. E. McMahon and D. J. Friedman are with the National Renewable Energy Laboratory, CO 80401 USA (e-mail: bill.mcmahon@nrel.gov; daniel.friedman@nrel.gov).

Color versions of one or more of the figures in this paper are available online at http://ieeexplore.ieee.org.

Digital Object Identifier 10.1109/JPHOTOV.2014.2304359

ARC is designed to minimize reflection into the underlying semiconductor.

The design and fabrication of a hybrid ARC was detailed in our paper published in the proceedings of the 39th IEEE Photovoltaics Specialist Conference. Here, we report on two significant results that were not discussed in the conference proceedings [16].

1) We model the performance of each ARC design as a function of both wavelength and angle of incidence. Results indicate that the hybrid ARC can reduce reflections across a wide angular range, with the greatest improvements occurring at the widest angles. This suggests that in addition to the enhancement in performance at normal incidence, the hybrid ARC should further improve the efficiency of an optical system which has a wide angular distribution.
2) Data from three different ARC designs are integrated into a detailed balance model to relate ARC performance to solar cell efficiency. We find that the AM1.5D weighted reflectance of an ARC is closely correlated to the modeled cell efficiency. This illustrates the importance of ARC design and suggests that minimizing reflected power for a given spectrum is a good design rule for photovoltaic applications.

II. Optical Modeling

A. Modeling Details

The design of a hybrid moth-eye ARC is compared with a multilayer ARC, a two-layer ARC, and no ARC for 3-J and 4-J designs. It is important to constrain each approach to the same parameter space so a fair comparison can be made.

For the 3-J design, we assume a bottom junction with a bandgap of 1.0 eV since this is similar to what is used for the highest efficiency 3-J device architectures. For the 4-J design, we assume a bottom junction consisting of 0.66-eV germanium, which is representative of the bottom junction bandgap for many proposed 4-J devices [2], [4], [5].

Material constraints are also important when comparing the design of each ARC. For the interference-based ARC layers, SiO_2 and TiO_2 are used. Due to their low ($n \approx 1.5$ for SiO_2) and high ($n \approx 2.7$ for TiO_2) indices of refraction, ARCs consisting of alternating layers of these two materials often outperform other combinations. All of the ARCs are optimized at normal incidence to minimize AM1.5D reflected power into indium gallium phosphide (InGaP). This material was chosen because it has a high refractive index that is representative of many III–V materials used in 3-J and 4-J architectures. All of the optical constants used for these models were obtained from the Sopra optical database [4], [5], [17], [18].

While typical multijunction photovoltaic devices have a very complicated optical structure, it is beneficial to compare the designs using a simpler configuration so that the quality of each ARC can be considered in a more general manner. The relative performance for each approach is expected to carry over for photovoltaic devices that incorporate different materials in the ARC and epitaxial structure.

The layer thicknesses for each of the three ARC designs were optimized using TFCalc from Software Spectra. Since the solar spectrum is not flat and covers a very broad range of wavelengths, the optical design is complex and nonintuitive. After performing a global search to find possible minimums in the design, the simplex optimization method is used to fine tune the thickness of each layer by minimizing a merit function describing the quality of the ARC. Designs with eight-layers were used as the starting point for optimization for both the multilayer and hybrid ARC [17], [19].

Under the simplifying assumption that the internal quantum efficiency (IQE) of the device is unity for all wavelengths larger than the bandgap of the bottom junction, the merit function is described as

$$F = \int_{\lambda_L}^{\lambda_H} I(\lambda)\, C(\lambda) d\lambda \tag{1}$$

where λ_L and λ_H describe the wavelength range over which the device is absorbing light, $C(\lambda)$ is the reflectance calculated using the transfer-matrix method, and $I(\lambda)$ is a weighting function that describes the power in the AM1.5D spectrum. This optimization will maximize the amount of energy coupled into the active layers.

For the hybrid ARC, the layer thicknesses are optimized independent from the geometry of the nanostructures. However, it is important to note that the height, period, and shape of the nanostructures can have a significant impact on the reflectivity of the full structure. The design and optimization of antireflective nanostructures are described in detail elsewhere, and greater than 99% transmission in SiO_2 across most of the solar spectrum has been reported [20]–[22].

B. Antireflection Coating Comparison

Table I shows the optimal structure for the interference-based ARC for each of the three designs. The layer to the far left is adjacent to InGaP and the layer to the far right is next to the nanostructured layer for the hybrid ARC and air for the multilayer and two-layer ARC.

After following the optimization procedure detailed earlier, a multilayer ARC with four-layers and a hybrid ARC with seven-layers turned out to have the lowest reflectivity. These two best case scenarios were used so that a fair comparison could be made.

Reflectance for each design is calculated using the transfer-matrix method. The optical properties of the nanostructured layer are modeled by calculating the effective index for 100 thin horizontal slices in the structure using the Bruggeman effective medium approximation [23], [24].

Cross-sectional scanning electron micrographs (SEMs) are used to estimate the shape of the fabricated nanostructures. The measured height of the moth-eye layer is about 750 nm. The fill factor, defined as the areal percent of SiO_2 in each slice, is approximated to be a linear function of height.

Weighting reflectance to the AM1.5D spectrum allows us to calculate the total reflected power for each design. These results are summarized in Table II. Splitting reflected power

TABLE I
ANTIREFLECTION COATING DESIGNS

ARC Design	Designs for 3-Junction Range (300 nm-1240 nm)							Designs for 4-Junction Range (300 nm-1879 nm)						
	InGaP → Incident Medium							InGaP → Incident Medium						
2-Layer ARC	**TiO_2**		**SiO_2**					**TiO_2**		**SiO_2**				
Thickness (nm)	38.82		98.59					40.22		101.67				
Multilayer ARC	**TiO_2**	**SiO_2**	**TiO_2**	**SiO_2**				**TiO_2**	**SiO_2**	**TiO_2**	**SiO_2**			
Thickness (nm)	39.03	21.85	12.72	96.10				43.42	24.20	14.39	104.71			
Hybrid ARC	**TiO_2**	**SiO_2**	**TiO_2**	**SiO_2**	**TiO_2**	**SiO_2**	**TiO_2**	**TiO_2**	**SiO_2**	**TiO_2**	**SiO_2**	**TiO_2**	**SiO_2**	**TiO_2**
Thickness (nm)	43.65	17.58	18.84	33.45	9.24	45.77	3.12	46.44	17.30	20.97	33.87	11.10	48.71	4.00

TABLE II
ANTIREFLECTION COATING COMPARISON

ARC Type	3-Junction Range (300 nm-1240 nm)		4-Junction Range (300 nm-1879 nm)	
	757.9 W/m^2 in this range in the AM1.5D Spectrum		*860.5 W/m^2 in this range in the AM1.5D Spectrum*	
	Reflected Power (W/m^2)	% of Power Reflected	Reflected Power (W/m^2)	% of Power Reflected
No ARC	**232.9**	**30.7%**	**260.3**	**30.3%**
2-Layer ARC	**38.8**	**5.1%**	**55.4**	**6.4%**
Multilayer ARC	**16.5**	**2.2%**	**26.5**	**3.1%**
Hybrid ARC	**4.7**	**0.6%**	**8.2**	**1.0%**

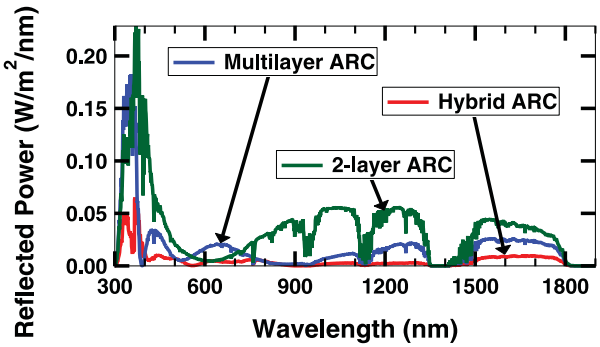

Fig. 2. Plot showing reflected power vs. wavelength for each ARC design across the 4-J wavelength range.

into individual wavelength components allows us to obtain a reflected power spectrum, which illustrates many important features from each design. This plot is shown in Fig. 2 for the three ARCs optimized to the 4-J wavelength range.

For the two-layer ARC, there is a region of very low reflected power centered near 600 nm. However, this region of low reflectivity does not cover the entire solar spectrum, leading to a high power reflection at short and long wavelengths. A multilayer ARC improves broadband performance because additional layers help to expand the design space.

The best performing design is the hybrid ARC. Historically, optical coatings have been constrained by the lack of materials with an index of refraction lower than MgF_2 ($n \approx 1.38$). By bridging the refractive index gap between air and SiO_2, the moth-eye coupling layer eliminates this constraint and opens up the potential for higher quality designs [17], [18].

C. Angular Characteristics of Antireflection Coatings

Since most terrestrial multijunction solar cells are used in conjunction with optical concentrator systems, it is important to consider the angular characteristics of each ARC.

The transfer-matrix method is used to calculate reflectance for both s and p polarized lights as a function of wavelength and angle. The results of these simulations for the 4-J designs are illustrated with contour plots in Fig. 3. The reflectance values shown are averaged from the s and p polarization components.

It is evident from these plots that the antireflective properties of the hybrid ARC are maintained across a wide angular range. This approach is less sensitive to angle for a couple of reasons. First, standalone moth-eye structures have excellent antireflective properties out to wide angles of incidence. Second, the reflectance from the interference-based ARC layers would not increase rapidly since the top moth-eye layer has the effect of refracting incident light from air to a shallower angle in SiO_2 due to Snell's law of refraction.

At normal incidence, we obtain the same values for reflected power as shown in Table II. At 45°, we find that the percentage of power reflected increases by an additional 1.3% for the two-layer ARC, 1.2% for the multilayer ARC, and less than 0.2% for the hybrid ARC when compared with the normal incidence values shown in Table II. At 60°, reflected power increases by 5.3% for the two-layer ARC, 5.2% for the multilayer ARC, and less than 0.8% for the hybrid ARC.

It is important to note from Fig. 3 that ARC performance will not change significantly from the normal incidence value when the maximum angle of the system is small. However, for a concentrated photovoltaic (CPV) system that spans a wide angular range, the hybrid ARC should provide an added benefit compared with conventional interference-based designs.

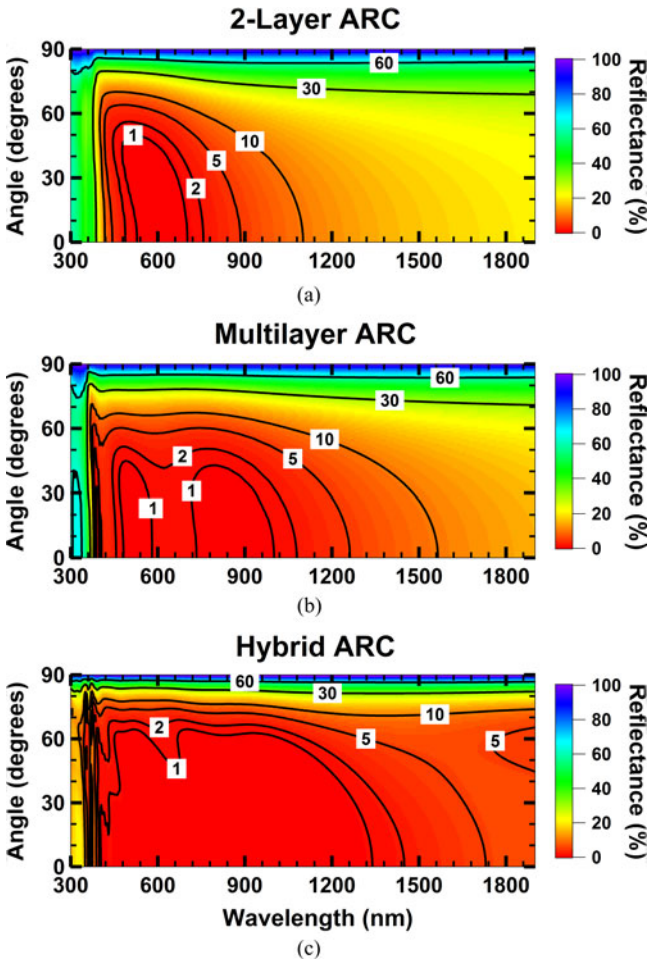

Fig. 3. Contour plots showing reflectance as a function of angle and wavelength for each ARC design.

D. Detailed Balance Cell Model

Reflectance for each of the three coatings is incorporated into a detailed balance model to correlate ARC design to solar cell efficiency. The model calculates the theoretical maximum efficiency for series-connected 3-J and 4-J architectures with bandgap combinations optimized for each configuration.

Some assumptions in the model include unity IQE, a concentration of 1000 suns, and a temperature of 300 K. For the 3-J case, the bandgap of the top junction is set to 1.9 eV, the bandgap of the middle junction is varied for optimization, and the bandgap of the bottom junction is set to 1.0 eV. For the 4-J case, the bandgap of the top junction is set at 1.9 eV, the bandgap of the second and third junctions is varied to maximize efficiency, and the bandgap of the bottom junction is set to 0.66 eV. The junctions are allowed to be thinned when necessary to pass light to the next junction [5].

Fig. 4 shows the results from this model. We see that there is an excellent correlation between the AM1.5D reflected power for each ARC and the modeled cell efficiency, with a coefficient of determination (R^2) of 0.9994 for the 4-J case and 0.9985 for the 3-J case. The optimal bandgaps of the middle junctions are slightly different for each design, which accounts for the nonunity R^2 value.

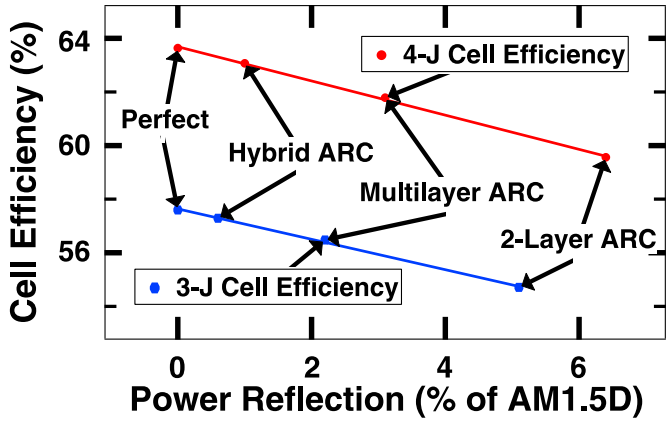

Fig. 4. Detailed balance model showing the correlation between AM1.5D reflected power and modeled cell efficiency at 1000 suns concentration, the two lines are linear fits to the data.

While the absolute efficiencies from this model are for idealized cells and therefore may not be possible to achieve, the relative values are useful for device design. Furthermore, they highlight the impact of ARC design on cell efficiency.

III. Results and Discussion

Each ARC design is fabricated on a sample consisting of approximately 1 μm of InGaP on a gallium arsenide (GaAs) substrate grown by metalorganic vapour phase epitaxy. The reflectance of the resulting coatings is measured and compared with simulations.

It is important to note that the optical constants reported in the Sopra optical database are not universal to each material. Of particular importance to our design, we find that the measured refractive index of our InGaP layer is a few percent higher and the refractive index of our TiO_2 film is a few percent lower than the values reported. For this reason, it is necessary to carefully characterize each material and reoptimize the designs prior to depositing the ARCs.

A. Experimental Details

All of the interference-based ARC layers are deposited using a VEECO ion beam-assisted sputter deposition system. For the hybrid ARC, an additional layer of SiO_2 is deposited with a thickness of approximately 1.5 μm to accommodate the antireflective nanostructures.

The moth-eye pattern is transferred from a nickel master stamp to the sample using thermal nanoimprint lithography. The stamp was fabricated by NIL Technology with the nanostructures arranged in a hexagonal array. The geometry of the moth-eye pattern is shown in the SEMs in Fig. 5.

The imprinting of the overlying resist layer is carried out at a pressure of 450 psi and a temperature of 140 °C using a Nanonex imprinting tool. The pattern is then transferred into the SiO_2 layer using an inductively-coupled plasma (ICP) etch. It is possible to have some control over the aspect ratio by adjusting the etch parameters. Using a 300-W CHF_3 etch, we achieve a SiO_2/resist etching ratio greater than 2:1.

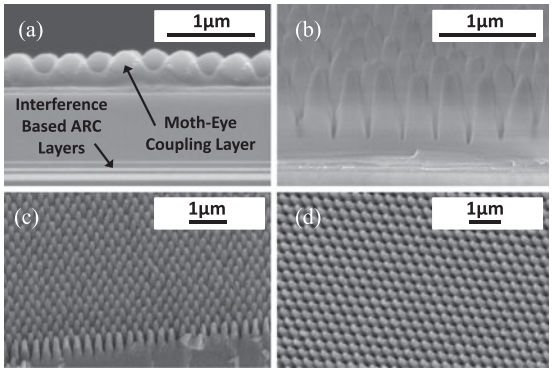

Fig. 5. SEMs of the hybrid moth-eye design. (a) Cross-sectional SEM showing the multilayer ARC and imprinted moth-eye pattern. (b) SEM of the sample after the ICP etch. (c) SEM of the sample showing excellent replication of the moth-eye pattern. (d) Top view SEM showing the hexagonal geometry of the nanostructures.

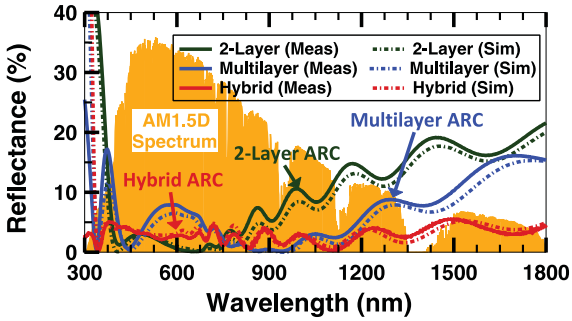

Fig. 6. Plot showing the measured and simulated reflectance for each ARC design at an angle of 8°.

Fig. 5(a) shows a cross-sectional SEM of the hybrid ARC after imprinting of the resist layer. The period and height of the moth-eye structure are approximately 350 nm. Fig. 5(b) shows the sample after the ICP etch and with the resist layer removed. This image allows us to estimate the geometry of the features for modeling their antireflective properties. The measured height of the moth-eye pattern is approximately 750 nm, and the fill factor appears to increase smoothly from the top of the structure to the bottom without any abrupt jump in the effective index of refraction.

Fig. 5(c) and (d) shows a larger section of the pattern after imprinting and etching. These images exhibit the excellent pattern fidelity of the final replicated structure.

B. Results

Specular reflectance for each ARC is measured using a Cary 500 UV-VIS-NIR spectrophotometer. These reflectance scans are compared with optical models.

Fig. 6 shows this comparison for each design. While the measurements do not account for diffuse reflections, close agreement between simulated and measured specular reflectance can provide indirect evidence that the moth-eye layer is not scattering a significant amount of light.

The simulations and optimized ARC designs take into account the interface between InGaP and GaAs. This interface

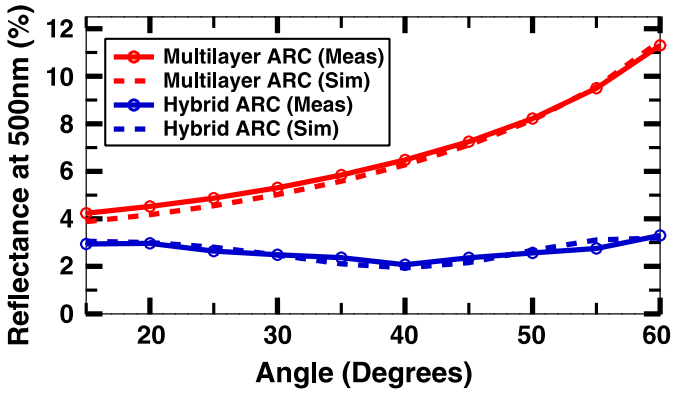

Fig. 7. Plot showing the measured and simulated reflectance for the hybrid and multilayer ARC at a wavelength of 500 nm.

is responsible for the interference fringes that begin around 675 nm, corresponding to the bandgap of InGaP. The period of these fringes is linked to the InGaP layer thickness.

Since the merit function is weighted to the direct spectrum, a measure of reflected AM1.5D power will provide a good comparison between each design. Using this metric, we find that the hybrid ARC performs much better than the other two designs.

The two-layer ARC specularly reflects 47.4 W/m^2, corresponding to 5.5% of the AM1.5D power in the 4-J wavelength range. The four-layer ARC reflects 38.6 W/m^2, or 4.5% of the power in the 4-J range. In comparison, the hybrid ARC specularly reflects just 24.0 W/m^2, corresponding to a 2.8% power reflection.

Note that the measured reflectance for the hybrid ARC starts to deviate from the simulated value below 350 nm. This occurs because these wavelengths are approaching the lateral dimensions of the nanostructures. Under these conditions, less light will be specularly reflected due to the onset of the first diffraction order of the moth-eye layer. Also note that if the nanostructures were scattering a significant amount of light at longer wavelengths, we could expect to see a similar disagreement between the measurements and the model [25].

A V-VASE ellipsometer is used to measure reflectance of the hybrid and multilayer ARC as a function of angle. Fig. 7 compares the measurements with our optical model from 15° to 60°. These values are acquired at a wavelength of 500 nm, and are averaged from s and p polarization data.

While Fig. 7 shows that the hybrid ARC maintains a lower reflectance than the multilayer ARC across the entire measured angular range, it is important to remember that these measurements are taken at a single wavelength. These data therefore do not show a full comparison between the two designs.

The most important result from Figs. 6 and 7 is that they show that the hybrid ARC is behaving very close to what we would expect from our optical model. They therefore represent an early indication that the relative efficiency improvements shown in Fig. 4 could be realized in practice for multijunction photovoltaics. We are currently working to integrate the hybrid ARC onto an active device to further characterize its performance.

C. Integration With Optical Elements and Cover Glass

A multijunction device will rarely be exposed to air when operated in the field. Typically, the device will be encapsulated with either coverglass when operated in space or a secondary optic when used in CPV systems. It is important to note that the hybrid approach should be compatible with both space and CPV systems.

For these applications, the antireflective nanostructures can be incorporated onto the front of the encapsulant since the thickness of the coupling layer is not critical to the hybrid design. As long as the nanostructures do not scatter or diffract incoming light, they will not affect the optics of the system.

Since superior optical design can be achieved by bridging the air–SiO_2 index gap, efficiencies for research cells with an ARC designed to air may be 1–2% lower than what can be achieved in the field if antireflective nanostructures are integrated into the optical system.

Antireflective nanostructures have already been developed for many commercial products, including wide-angle camera lenses and 80-in television displays. Adoption of the same nanoimprinting process for photovoltaic systems should lead to notable improvements in optical efficiency for CPV and space photovoltaics.

IV. Conclusion

In this study, we present a novel ARC design which integrates a nanostructured antireflection layer with a multilayer interference-based dielectric stack. This approach is compared with multilayer and two-layer ARC designs. Optical models show that the hybrid ARC can reduce reflected AM1.5D power by 10–50 W/m^2 compared with two-layer and multilayer ARCs. Furthermore, they exhibit better broadband and wide-angle performance.

The three ARCs were fabricated on a sample consisting of approximately 1μm of InGaP on GaAs. Reflectance scans show a 1.7% and 2.7% decrease in AM1.5D reflected power percentage versus multilayer and two-layer ARCs, respectively. This translates to an improvement of roughly 1–2% in cell efficiency for a 40% efficient multijunction device.

Acknowledgment

The authors would like to thank A. Kibbler for assistance with the epitaxial growth of the InGaP/GaAs samples, R. Farrell for valuable discussions about the design and deposition of the antireflection coatings, and B. Thibeault for excellent guidance with developing the fabrication process.

References

[1] M. A. Green, K. Emery, Y. Hishikawa, W. Warta, and E. D. Dunlop, "Solar cell efficiency tables (version 42)," *Progress Photovoltaics, Res. Appl.*, vol. 21, no. 5, pp. 827–837, 2013.

[2] D. C. Law, R. R. King, H. Yoon, M. J. Archer, A. Boca, C. M. Fetzer, S. Mesropian, T. Isshiki, M. Haddad, K. M. Edmondson, D. Bhusari, J. Yen, R. A. Sherif, H. A. Atwater, and N. H. Karam, "Future technology pathways of terrestrial III–V multijunction solar cells for concentrator photovoltaic systems," *Sol. Energy Mater, Sol. Cells*, vol. 94, no. 8, pp. 1314–1318, 2010.

[3] D. J. Aiken, "High performance anti-reflection coatings for broadband multi-junction solar cells," *Sol. Energy Mater. Sol. Cells*, vol. 64, no. 4, pp. 393–404, 2000.

[4] R. R. King, A. Boca, W. Hong, X.-Q. Liu, D. Bhusari, D. Larrabee, K. M. Edmondson, D. C. Law, C. M. Fetzer, S. Mesropian, and N. H. Karam, "Band-gap-engineered architectures for high-efficiency multijunction concentrator solar cells," in *Proc. 24th Eur. Photovoltaic Solar Energy Conf. Exhib.*, 2009, vol. 21.

[5] D. J. Friedman, J. M. Olson, and S. R. Kurtz, "High-efficiency III-V multijunction solar cells," in *Handbook of Photovoltaic Science and Engineering*, 2nd ed. A. Luque and S. Hegedus, Eds. Chichester, U.K.: Wiley, 2011, pp. 314–364.

[6] P. T. Chiu, D. C. Law, R. L. Woo, S. B. Singer, D. Bhusari, W. D. Hong, A. Zakaria, J. Boisvert, S. Mesropian, R. R. King, and N. H. Karam, "Direct semiconductor bonded 5J cell for space and terrestrial applications," *IEEE J. Photovoltaics*, vol. 4, no. 1, pp. 493–497, 2014.

[7] C. G. Bernhard, "Structural and functional adaptation in a visual system," *Endeavor*, vol. 26, no. 98, pp. 79–84, 1967.

[8] S. J. Wilson and M. C. Hutley, "The optical properties of moth eye antireflection surfaces," *J. Modern Opt.*, vol. 29, no. 7, pp. 993–1009, 1982.

[9] J. Zhu, C.-M. Hsu, Z. Yu, S. Fan, and Y. Cui, "Nanodome solar cells with efficient light management and self cleaning," *Nano Lett.*, vol. 10, no. 6, pp. 1979–1984, 2009.

[10] Y. Kang, D. Liang, Y. Huo, A. Gu, S. Li, Y. Chen, and J. Harris, "Design and fabrication of nano-pyramid GaAs solar cell," in *Proc 39th IEEE Photovoltaic Spec. Conf.*, 2013, to be published.

[11] J. Tommila, A. Aho, A. Tukiainen, V. Polojärvi, J. Salmi, T. Niemi, and M. Guina, "Moth-eye antireflection coating fabricated by nanoimprint lithography on 1 eV dilute nitride solar cell," *Progress Photovoltaics, Res. Appl.*, vol. 21, no. 1, pp. 1158–1162, 2013.

[12] D. Liang, Y. Kang, Y. Huo, Y. Chen, Y. Cui, and J. S. Harris, "High-efficiency nanostructured window GaAs solar cells," *Nano Lett.*, vol. 13, no. 10, pp. 4850–4856, 2013.

[13] J. Tommila, V. Polojärvi, A. Aho, A. Tukiainen, J. Viheriälä, J. Salmi, A. Schramm, J. M. Kontio, A. Turtiainen, T. Niemi, and M. Guina, "Nanostructured broadband antireflection coatings on AlInP fabricated by nanoimprint lithography," *Sol. Energy Mater. Sol. Cells*, vol. 94, no. 10, pp. 1845–1848, 2010.

[14] K.-H. Hung, T.-G. Chen, T.-T. Yang, P. Yu, C.-Y. Hong, Y.-R. Wu, and G.-C. Chi, "Antireflective scheme for InGaP/InGaAs/Ge triple junction solar cells based on TiO2 biomimetic structures," in *Proc 38th IEEE Photovoltaic Spec. Conf.*, 2012, pp. 003322–003324.

[15] P. Yu, M.-Y. Chiu, C.-H. Chang, C.-Y. Hong, Y.-L. Tsai, H.-V. Han, and Y.-R. Wu, "Towards high-efficiency multi-junction solar cells with biologically inspired nanosurfaces," *Progress Photovoltaics, Res. Appl.*, 2012, doi: 10.1002/pip.2259.

[16] E. E. Perl, C.-T. Lin, W. E. McMahon, D. J. Friedman, and J. E. Bowers, "Design of ultra-broadband antireflection coatings utilizing integrated moth-eye structures for multi-junction device applications," in *Proc 39th IEEE Photovoltaic Spec. Conf.*, 2013, to be published.

[17] H. A. Macleod, *Thin-Film Optical Filters*. Boca Raton, FL, USA: CRC Press, 2001, ch. 4.

[18] Refractive Index Database, (2011, Dec.) [Online]. Available: http://refractiveindex.info

[19] *TFCalc Version 3.5.15*, Software Spectra, Inc., Portland, OR, USA, 2009.

[20] Y. M. Song, H. J. Choi, J. S. Yu, and Y. T. Lee, "Design of highly transparent glasses with broadband antireflective subwavelength structures," *Opt. Exp.*, vol. 18, no. 12, pp. 13063–13071, 2010.

[21] G. C. Park, Y. M. Song, E. K. Kang, and Y. T. Lee, "Size-dependent optical behavior of disordered nanostructures on glass substrates," *Appl. Opt.*, vol. 51, no. 24, pp. 5890–5896, 2012.

[22] D. S. Hobbs, B. D. MacLeod, and J. R. Riccobono, "Update on the development of high performance anti-reflecting surface relief microstructures," in *Proc. SPIE*, 2007, vol. 6545, p. 65450Y.

[23] D. G. Stavenga, S. Foletti, G. Palasantzas, and K. Arikawa, "Light on the moth-eye corneal nipple array of butterflies," *Proc. Roy. Soc. B, Biol. Sci.*, vol. 273, no. 1587, pp. 661–667, 2006.

[24] D. A. G. Bruggeman, "Calculation of various physics constants in heterogeneous substances: Part I. Dielectric constants and conductivity of mixed bodies from isotropic substances," *Annalen der Physik*, vol. 24, no. 7, pp. 636–664, 1935.

[25] P. I. Stavroulakis, S. A. Boden, T. Johnson, and D. M. Bagnall, "Suppression of backscattered diffraction from sub-wavelength 'moth-eye' arrays," *Opt. Exp.*, vol. 21, no. 1, pp. 1–11, 2013.

Authors' photographs and biographies not available at the time of publication.